Available online at www.sciencedirect.com
ScienceDirect
Trans. Nonferrous Met. Soc. China 32(2022) 2696−2708
Transactions of Nonferrous Metals Society of China
www.tnmsc.cn

Failure process and characteristics of three-dimensional high-stress circular tunnel under saturated water content

Xue-feng SI[1], Lin-qi HUANG[1], Feng-qiang GONG[2], Xi-bing LI[1]

1. School of Resources and Safety Engineering, Central South University, Changsha 410083, China;
2. School of Civil Engineering, Southeast University, Nanjing 211189, China

Received 9 August 2021; accepted 18 February 2022

Abstract: True-triaxial compression tests were carried out on cubic granite samples with a circular through hole using a true-triaxial testing system to investigate the influence of saturated water content (SWC) on the failure process and characteristics of a circular tunnel of surrounding rocks. The spalling failure under SWC can be divided into four periods: calm period, buckling deformation period, period of rock fragment gradual buckling and exfoliation, and period of formation of symmetrical V-shaped notches. When the horizontal axial and vertical stresses were constant, the spalling failure severity was reduced with the increase in lateral stress. Under natural water content, a strong rockburst with dynamic failure characteristics occurred on the circular hole sidewall. Under SWC, the failure severity was reduced and the circular hole sidewall experienced spalling failure, exhibiting progressive static failure characteristics. Therefore, water can reduce the failure severity of surrounding rocks in deep underground engineering, which has a certain guiding significance for the prevention and control of rockbursts.

Key words: deep hard rock; circular tunnel; saturated water content; rockburst; spalling failure; three-dimensional high-stress; V-shaped notch

1 Introduction

In deep underground engineering, the rock mass is in a complex environment with a high geostress and groundwater [1,2]. In the water-rich stratum, water has a certain influence on the mechanical properties of rocks. Under normal circumstances, the water content can reduce the strength and elastic brittleness of rocks, which in turn makes the rocks more prone to damage [3−5]. Extensive studies have been carried out on the influence of the water content on the physical and mechanical properties of rocks [6−9]. MASOUMI et al [6] reported that the uniaxial compressive strength (UCS), elastic modulus, point-load index, and tensile strength of Gosford sandstone decreased with the increase in water content. ZHOU et al [7] carried out dynamic tests on both dry and saturated sandstone samples and reported that the saturated rock samples exhibited stronger rate dependence than the dry samples. BAUD et al [8] carried out triaxial compression experiments on the four sandstones and compared the water-weakening effect. TAIBI et al [9] investigated the effect of suction on the hydromechanical behavior of a partially saturated soft rock under a low confining stress. The above studies mainly focused on the influence of the water content on the mechanical properties of rocks under uniaxial and triaxial compression conditions.

In deep hard rocks under a high stress state, rockburst and spalling failure often occur, which threatens the safety of underground personnel and equipment and seriously affects the normal progress of project construction [10−13]. Extensive studies

Corresponding author: Lin-qi HUANG, Tel: +86-13469059806, E-mail: huanglinqi@csu.edu.cn
DOI: 10.1016/S1003-6326(22)65976-4

have been carried out on the failure process and characteristics of deep tunnel surrounding rocks under natural water content (NWC) [14−18]. GONG et al [14,15] carried out spalling failure and rockburst simulation tests on cubic red sandstone and granite samples with a cylindrical hole and investigated the influence of the stress state on the severity of spalling failure and rockburst. SI et al [16,17] studied the rockburst characteristics of phyllite and granite and revealed the influence mechanism of the bedding angle and unloading rate via uniaxial compression and triaxial unloading compression tests. HU et al [18] analyzed rock fragmentation, failure, and acoustic emission characteristics by true-triaxial tests on cubic granite samples. In deep underground engineering, rockbursts rarely occur in rock masses with high water contents [19−21]. However, the influence of the water content on the failure characteristics of surrounding rocks in tunnels under true-triaxial stress conditions has not been extensively investigated.

In this study, true-triaxial compression tests were carried out using a true-triaxial testing system on cubic granite samples containing a circular through hole under a saturated water content (SWC). During the tests, the spalling failure of the circular hole sidewall was monitored and recorded in real time using a miniature camera. The failure process and characteristics were analyzed under SWC. The influence of the water content on the failure severity was discussed.

2 Experimental

2.1 Sample preparation

A fine-grained granite material was obtained from Zhangzhou City, Fujian Province, China. The mineral composition of the granite is approximately 49 wt.% quartz, 43 wt.% plagioclase, 4 wt.% biotite, 3 wt.% hornblende, and 1 wt.% opaque minerals, as shown in Fig. 1 [22,23]. The granite material was processed into cylindrical standard samples with dimensions of *d*50 mm × 100 mm and cubic samples with dimensions of 100 mm × 100 mm × 100 mm with a circular through hole (*d*=50 mm), as shown in Fig. 2. The machining precision was in strict accordance with the International Society for Rock

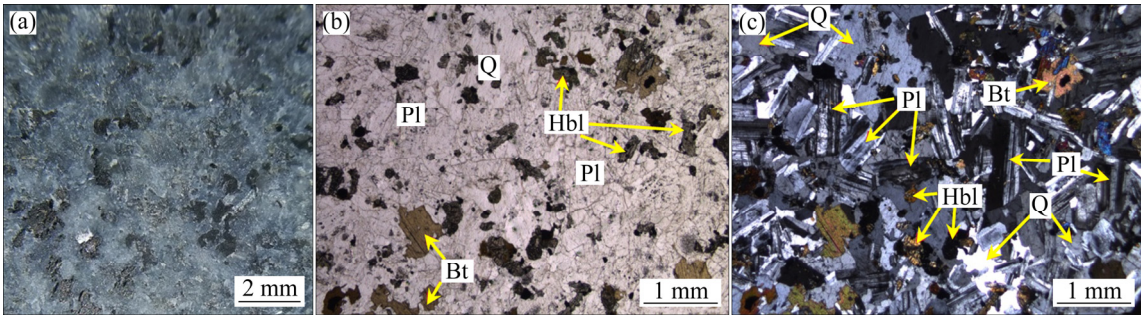

Fig. 1 Granite material: (a) Naked-eye observation [22]; (b) Plane-polarized light; (c) Cross-polarized light (Q, Pl, Bt, and Hbl represent quartz, plagioclase, biotite, and hornblende, respectively) [23]

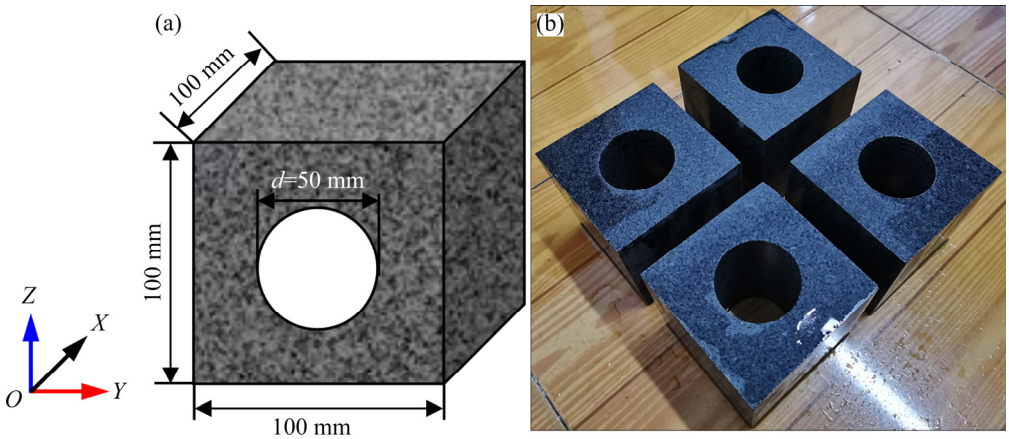

Fig. 2 Schematic of cubic granite sample (a), and photograph of saturated granite samples (b)

Mechanics Standards. The processed cubic granite samples were baked at a constant temperature of 105 °C for at least 24 h, and then cooled to room temperature (25 °C) in a desiccator. The dried samples were immersed in distilled water at room temperature for 48 h until the sample mass became constant (did not further increase), which indicated that the treated samples were in a saturated water state.

2.2 Experiment equipment

The true-triaxial testing system (Figs. 3(a) and (b)) was used for the indoor simulation tests. To monitor the failure of the circular hole sidewall, a circular through hole with a diameter of 50 mm was opened in the *X*-direction loading block, wherein an XM-JPG−4S microcamera (Fig. 3(c)) was installed, as shown in Fig. 3(d).

2.3 Stress path

The stresses in the three directions (*X*, *Y*, and *Z*) were increased to the preset stresses at the same loading rate of 1 kN/s using the load control method. The *X*-direction loading method was then changed to displacement control, and the *X*-direction displacement and *Y*-direction stress were kept constant (simulation of the plane strain problem). Subsequently, the *Z*-direction stress was continually increased by step loading at the same loading rate (stress adjustment was simulated by increasing the *Z*-direction stress). When a serious failure occurred on both sidewalls (the samples remained intact), the stresses in the three directions were unloaded to 0 MPa with a displacement rate of 20 mm/min after maintenance for a period. The stress paths involved in these tests are shown in Fig. 4.

To simulate the failure characteristics of the circular hole sidewall under SWC at a depth of 1 km, the initial stress state was calculated according to the distribution characteristics of in-situ stress [24,25]. The in-situ stresses can be expressed as

$$\begin{cases}\sigma_{\mathrm{v}}=0.027H\\ \sigma_{\mathrm{hmax}}=6.7+0.0444H\\ \sigma_{\mathrm{hmin}}=0.8+0.0329H\end{cases}$$

where σ_{v} is the vertical stress, σ_{hmax} is the maximum horizontal stress, σ_{hmin} is the minimum horizontal stress, and H is the depth. At a depth of 1 km, $\sigma_Z=\sigma_{\mathrm{v}}=27$ MPa, $\sigma_{\mathrm{hmax}}=51$ MPa, and $\sigma_{\mathrm{hmin}}=34$ MPa. The four combinations of the horizontal stresses σ_{hmax} and σ_{hmin} are shown in Fig. 5.

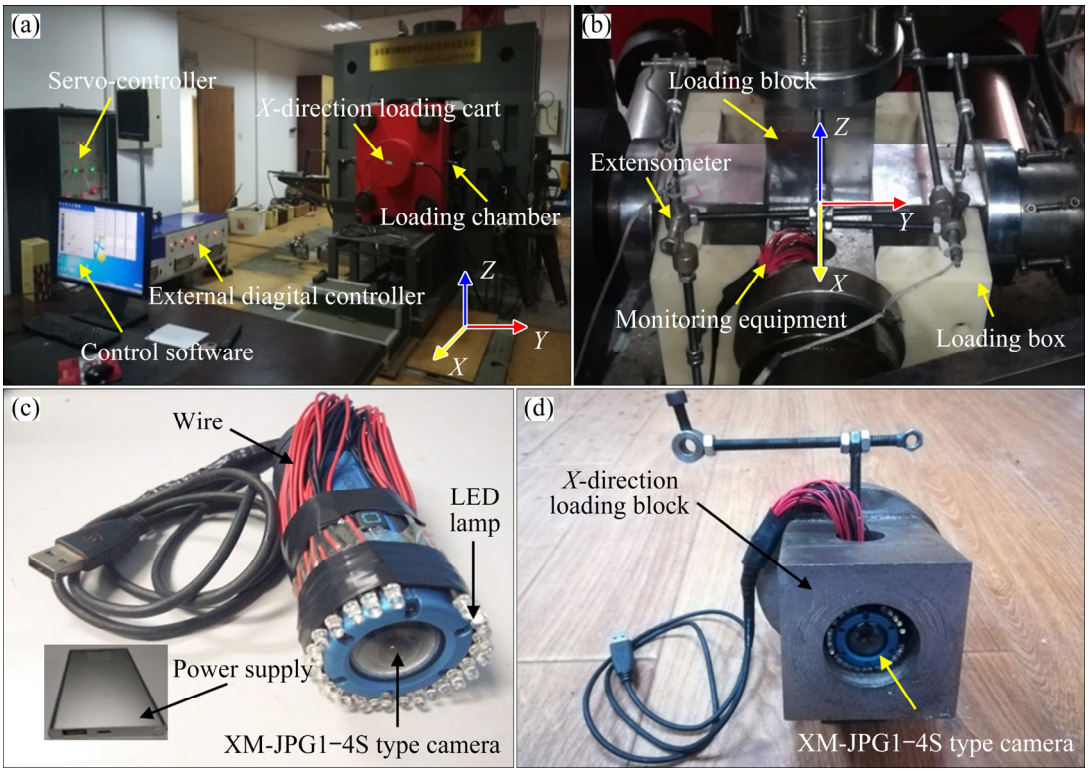

Fig. 3 Experimental equipment: (a) True-triaxial testing machine; (b) Cubic sample loading chamber; (c) XM-JPG1−4S microcamera; (d) Installation of microcamera in *X*-direction loading block

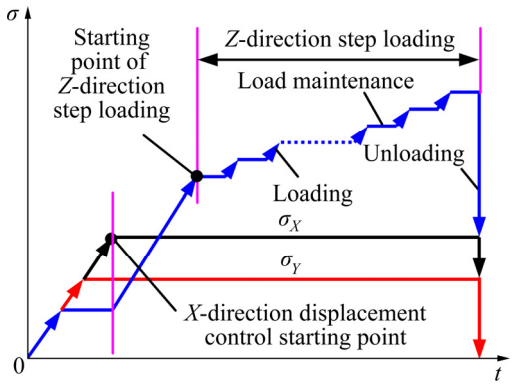

Fig. 4 Schematic of stress path

3 Results

3.1 Physical and mechanical properties of granite under different water contents

Under NWC, the average P-wave velocity, UCS, and elastic modulus of granite were 4.9 km/s, 261.6 MPa, and 57.9 GPa, respectively. The selected fine-grained granite belongs to the major rock categories used in laboratory experiments and is a typical hard rock [26]. To investigate the physical and mechanical properties of granite under SWC, the same saturation treatment of the cylindrical and cubic samples was carried out, as described in Section 2.1. The NWC and SWC of the granite were 0.15 wt.% and 0.49 wt.%, respectively. Under SWC, the average P-wave velocity, UCS, and elastic modulus were 6.1 km/s, 179.0 MPa, and 45.4 GPa, respectively. The P-wave velocity increased because the water filled the pores in the rock under SWC, which reduced the reflection, refraction, and diffraction of P-waves. The average UCS and elastic modulus of the granite samples under SWC decreased, which indicated that the water had significant reduction effects on the strength and brittleness.

3.2 Stress–time curves under true-triaxial compression

Figure 6 shows stress–time curves in the three directions. The *X*-direction stress exhibited slight fluctuations after shifting the load control to displacement control. The stresses in the *Z* direction of Samples HKW-34-34, HKW-34-51, HKW-51-34, and HKW-51-51 were increased to 152.0 MPa (Fig. 6(a)), 166.0 MPa (Fig. 6(b)), 150.0 MPa (Fig. 6(c)), and 166.0 MPa (Fig. 6(d)), respectively.

3.3 Failure process of circular hole sidewall under SWC

Sample HKW-34-34 was used as an example to describe the sidewall failure process in detail, as illustrated in Fig. 7. When the stresses in the three directions were increased to the preset stress states, there was no failure on both sidewalls. At 1114.24 s, the vertical stress σ_Z was loaded to 94.5 MPa and the right sidewall exhibited a slight buckling

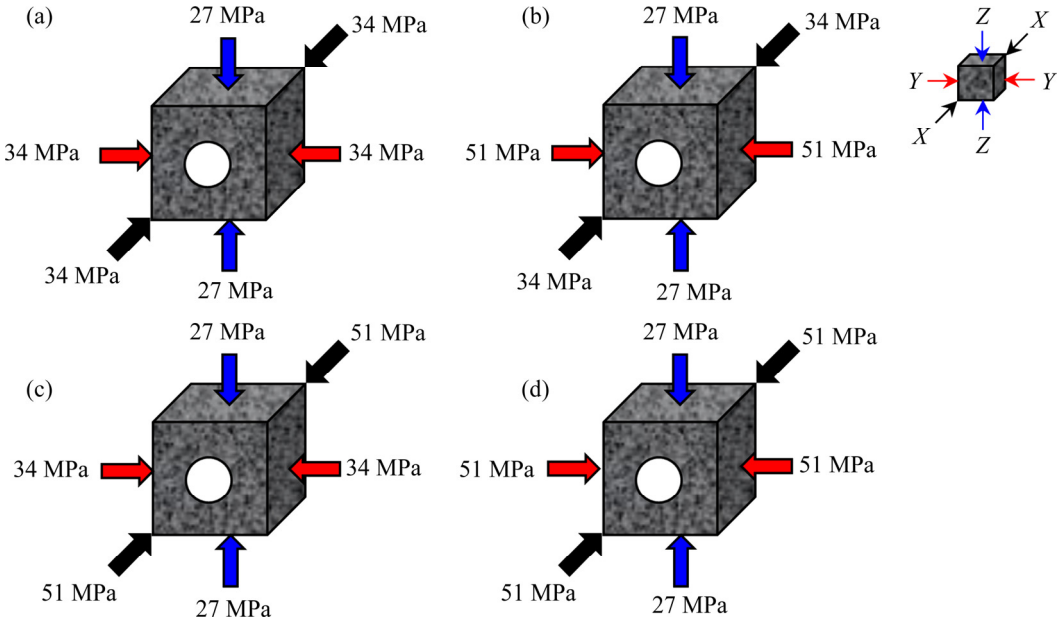

Fig. 5 Three-dimensional initial stress diagrams under four stress conditions: (a) HKW-34-34; (b) HKW-34-51; (c) HKW-51-34; (d) HKW-51-51

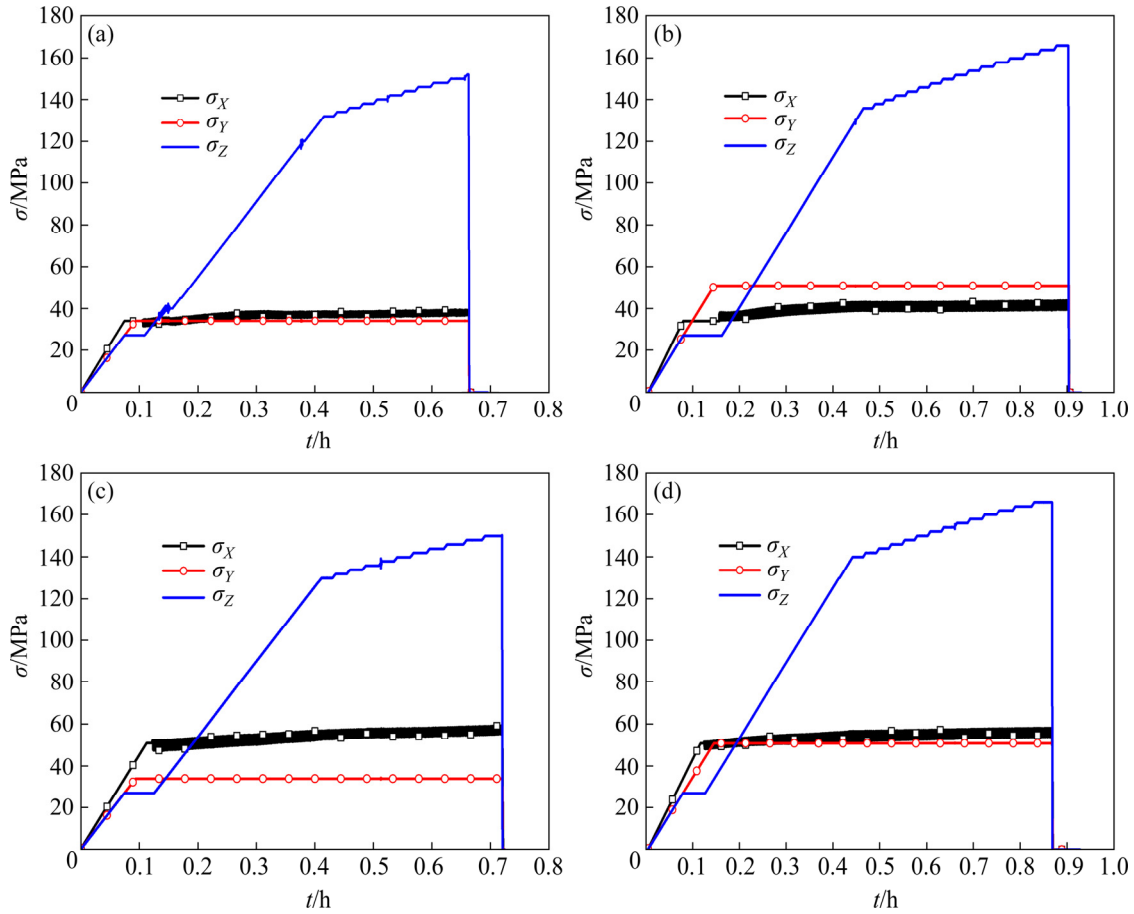

Fig. 6 Stress–time curves: (a) HKW-34-34; (b) HKW-34-51; (c) HKW-51-34; (d) HKW-51-51

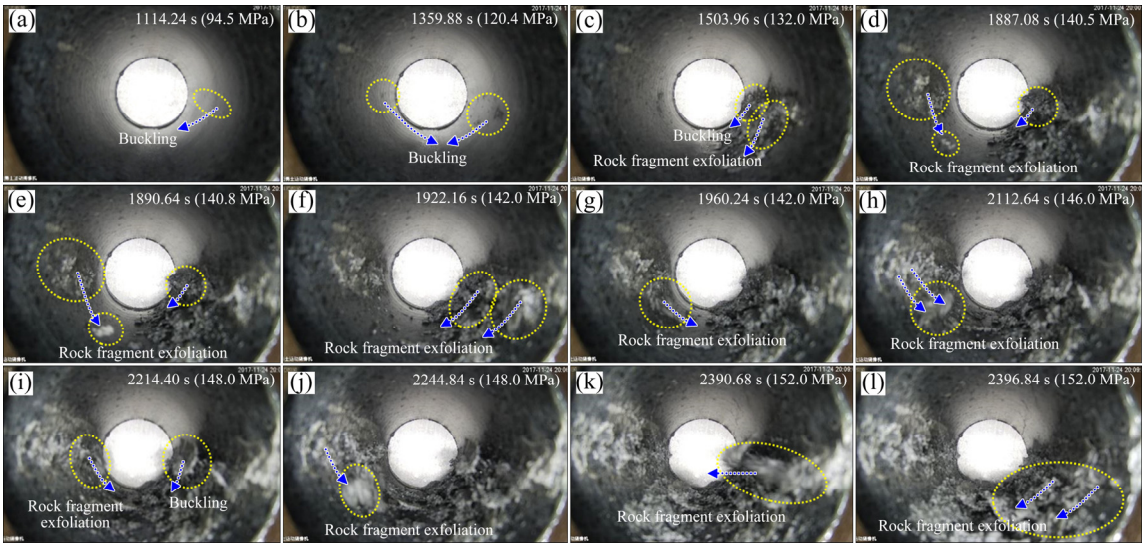

Fig. 7 Failure process of Sample HKW-34-34 under SWC

deformation, as shown in Fig. 7(a). When σ_Z= 120.4 MPa, buckling deformation occurred on the left sidewall and the rock fragments on the right sidewall gradually expanded to the free surface (Fig. 7(b)). When σ_Z=132.0 MPa, the right sidewall produced multiple rock fragment exfoliations, as shown in Fig. 7(c). When σ_Z was increased, multiple rock fragment exfoliations occurred on the right sidewall. When σ_Z=132.0 MPa, step loading was applied in the Z direction (maintained for approximately 1 min at each step), with a stress increment of 2.0 MPa. When σ_Z was increased to

140.5 and 140.8 MPa, fine rock fragment exfoliation occurred on the left sidewall and the rock fragments on the left and right sidewalls gradually buckled, as shown in Figs. 7(d) and (e), respectively. In Fig. 7(f), the different positions of the right sidewall simultaneously produced rock fragment exfoliations when σ_Z=142.0 MPa. When σ_Z was maintained at 142.0 MPa, a large rock fragment exfoliation occurred on the left sidewall at 1960.24 s, as illustrated in Fig. 7(g). At 2112.64 s, σ_Z was increased to 146.0 MPa and two adjacent rock fragments on the left sidewall simultaneously exfoliated (Fig. 7(h)). When σ_Z=148.0 MPa, the left sidewall produced rock fragment exfoliation, as shown in Fig. 7(i). When σ_Z was maintained at 148.0 MPa, the left sidewall produced a large rock fragment exfoliation (Fig. 7(j)). When σ_Z= 152.0 MPa, the right sidewall produced multiple rock fragment exfoliations, as shown in Figs. 7(k) and (l). Finally, the failure of the left and right sidewalls penetrated the sample along the direction of the hole axis.

The spalling failure processes of Samples HKW-34-51, HKW-51-34, and HKW-51-51 were similar to that of Sample HKW-34-34 under SWC. In summary, the spalling failure of the circular hole sidewall under SWC can be divided into four periods: calm period, buckling deformation period, period of rock fragment gradual buckling and exfoliation, and period of formation of symmetrical V-shaped notches. During the failure (Fig. 7), in the buckling deformation period, the rock fragment gradually buckled, while the exfoliation period lasted for a long time. A typical rock fragment on the right sidewall approximately in the middle position was selected to introduce the spalling process. At 1503.96 s, the rock fragment on the right sidewall produced a considerable buckling deformation (Fig. 7(c)). With the increase in vertical stress, this rock fragment gradually buckled and opened toward the free surface, as shown in Figs. 7(c−e). When the buckling deformation reached a certain degree, rock fragment exfoliation occurred, as illustrated in Fig. 7(f). The spalling of this rock fragment lasted for 418.20 s. This indicated that the energy in the surrounding rocks was slowly released during the buckling deformation. As shown in Fig. 7(f), when the rock fragment was exfoliated, there was no ejection. Therefore, the circular hole sidewall suffered from spalling failure with progressive static failure characteristics.

3.4 Failure characteristics of circular hole sidewall under SWC

Failure photographs of the samples are shown in Fig. 8. Overall, the samples were not unstable. Approximately symmetrical V-shaped notches were formed on both sidewalls. The locations and shapes of the V-shaped failure zones under the four initial stress states were similar. As shown in Fig. 8, the exfoliated rock fragments on both sidewalls were distributed in the two areas at the hole floor. For example, the rock fragments from the left sidewall were distributed in the left area of the floor, while the rock fragments from the right sidewall were distributed in the right area of the floor. Little kinetic energy was released when the rock fragments were exfoliated, exhibiting progressive static spalling failure characteristics. According to the failure process described in Section 3.3, partial rock fragments were exfoliated, while the remaining part did not separate from the surrounding rock, mainly as the water reduced the brittleness of the rock. Therefore, a large buckling deformation was prone to occur. The energy accumulated in the surrounding rock was slowly released, which resulted in little kinetic energy when the rock fragments were exfoliated. For rock fragments in the inner layer, no exfoliations were observed. In actual engineering, rock fragments that have no complete exfoliation should be cleaned to prevent safety threats to construction personnel and equipment caused by completely exfoliated rock fragments.

Figure 9 shows the characteristics of the rock fragments removed from the circular holes. The rock fragments under the four stress states were thick in the middle and thin at the edge. When the lateral stress (Y-direction stress) was 34.0 MPa, the length of rock fragments was relatively large. The longest rock fragments had sizes of approximately 62 mm (Fig. 9(a)) and 82 mm (Fig. 9(c)). When the lateral stress was 51.0 MPa, the length of the rock fragments was relatively small. The longest rock fragments had sizes of approximately 30 mm (Fig. 9(b)) and 35 mm (Fig. 9(d)). Therefore, the left and right sidewalls produced larger rock fragments under SWC when the lateral stress was lower.

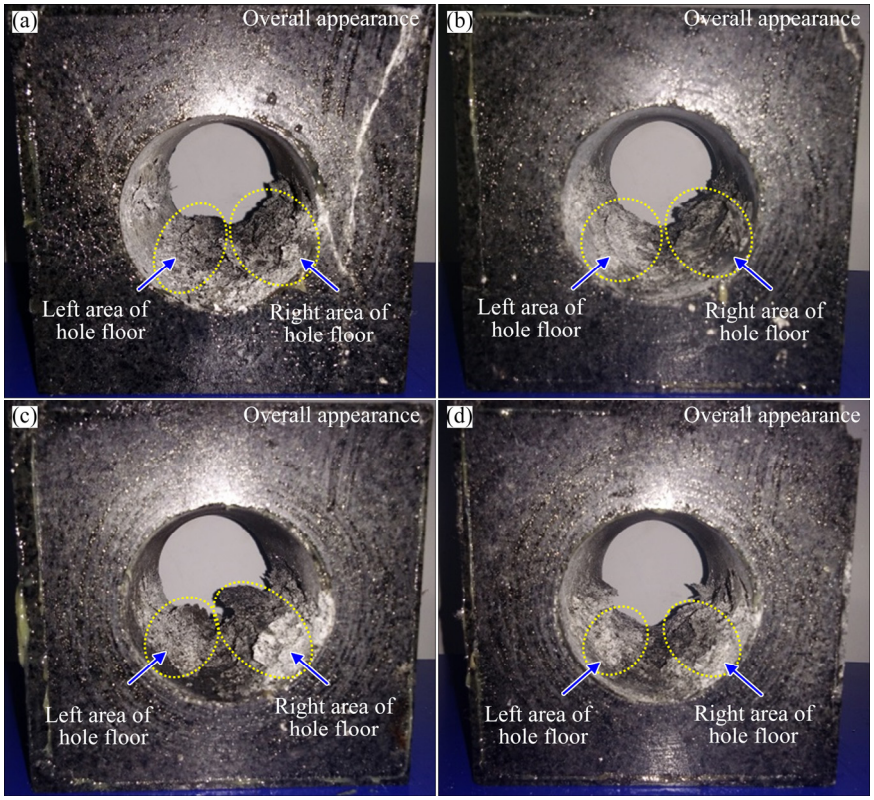

Fig. 8 Failure photographs of samples under SWC: (a) HKW-34-34; (b) HKW-34-51; (c) HKW-51-34; (d) HKW-51-51

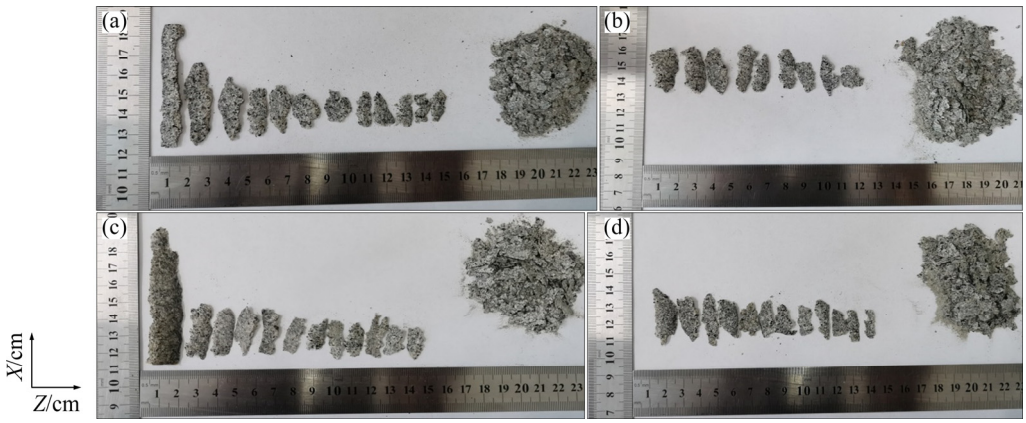

Fig. 9 Rock fragments under different stress states: (a) HKW-34-34; (b) HKW-34-51; (c) HKW-51-34; (d) HKW-51-51

4 Discussion

4.1 Evolution process of sidewall failure under SWC

The spalling failure under SWC can be divided into four periods with increasing vertical stress: calm period, buckling deformation period, period of rock fragment gradual buckling and exfoliation, and period of formation of symmetrical V-shaped notches. The failure characteristics in each period can be summarized as follows.

(1) Calm period: The sidewall remained intact, while the surrounding rock was compacted. The water in the pores of the surrounding rock was partially discharged from the free surface. With the increase in vertical stress, large amount of strain energy was stored and accumulated in the surrounding rock, while microcracks were generated and expanded. This period was the incubation period for the sidewall failure. A schematic diagram of this process is shown in Fig. 10(a).

(2) Buckling deformation period: The left and

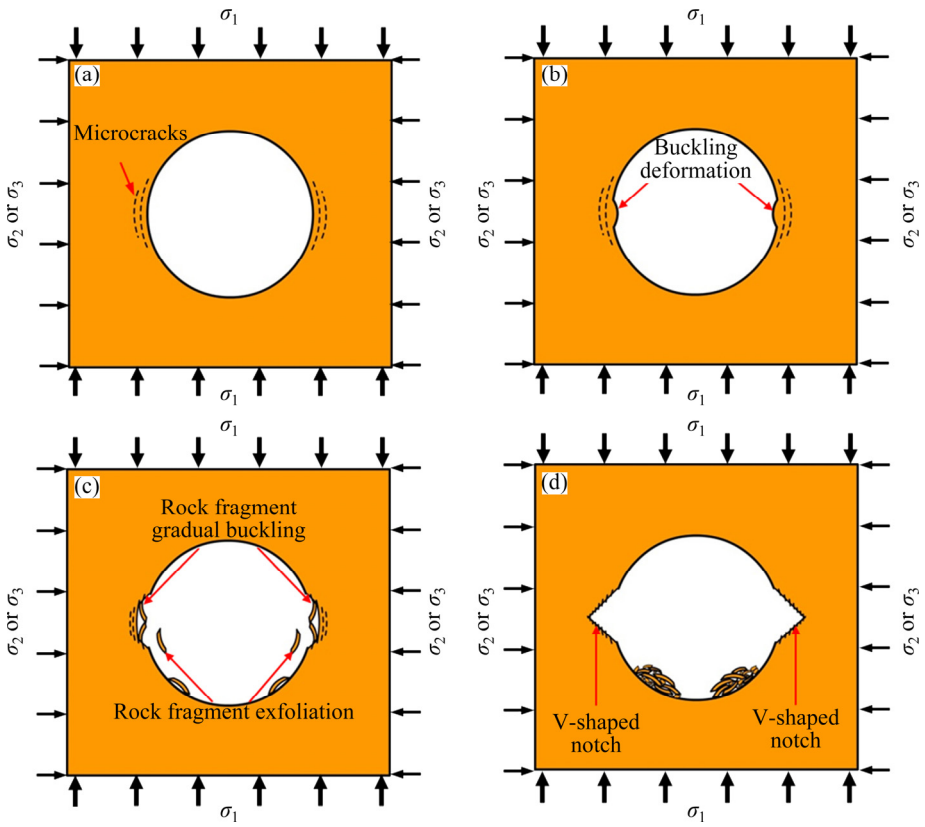

Fig. 10 Schematic diagrams of failure evolution process of circular hole sidewall under SWC: (a) Calm period; (b) Buckling deformation period; (c) Period of rock fragment gradual buckling and exfoliation; (d) Period of formation of symmetrical V-shaped notches (σ_1, σ_2, and σ_3 are the maximum, intermediate, and minimum principal stresses, respectively)

right sidewalls were high-stress concentration zones. The brittleness of the surrounding rock was reduced under SWC. Therefore, the sidewall exhibited a buckling deformation toward the free surface. With the increase in vertical stress, multiple buckling deformations occurred on the sidewall at different positions and gradually expanded and penetrated along the hole axis. A schematic diagram of this process is shown in Fig. 10(b).

(3) Period of rock fragment gradual buckling and exfoliation: When the vertical stress was increased to a higher stress state, the rock fragments gradually buckled and expanded toward the free surface. This period presented a progressive failure characteristic. After buckling, expansion to a certain extent, and reaching their bearing limit, the rock fragments were exfoliated. The exfoliation processes of the rock fragments exhibited low or almost zero kinetic energy. Therefore, the exfoliated rock fragments on both sidewalls were distributed in the two areas at the hole floor. The rock fragments from the left sidewall were distributed in the left area of the hole floor, while the rock fragments from the right sidewall were distributed in the right area of the hole floor, as shown in Fig. 10(c).

(4) Period of formation of symmetrical V-shaped notches: With further increase in vertical stress, the failure of both sidewalls under SWC expanded to the depth of the surrounding rock. Finally, symmetrical V-shaped notches were formed on both sidewalls, as shown in Fig. 10(d).

During the sidewall failure, two or more of the four periods were simultaneously observed at different positions, particularly under a high vertical stress, as shown in Figs. 7(f, h, i). This indicated that the sidewall failure had spatial distribution characteristics.

4.2 Influence of stress state on sidewall failure under SWC

Figure 11 shows the sidewall failure of the circular hole under SWC and different stress states, wherein the vertical stress was 130.0 and 150.0 MPa, respectively. For Sample HKW-34-34, when σ_Z=130.0 MPa, obvious buckling deformation

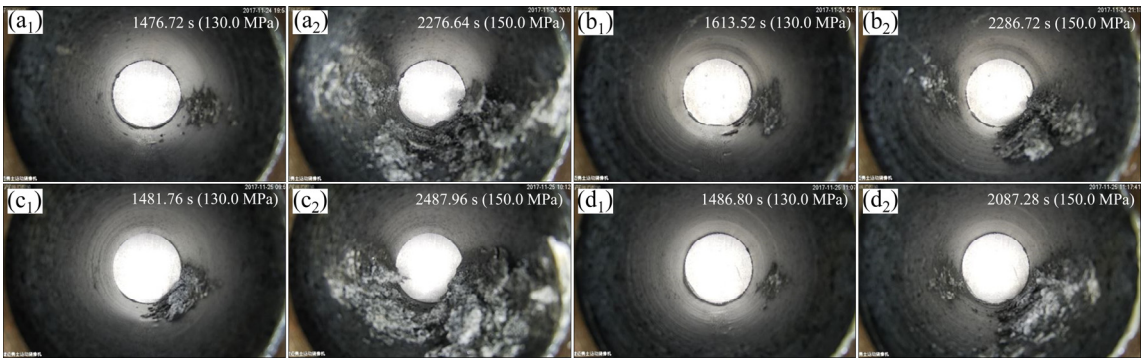

Fig. 11 Failure severity of circular hole sidewalls under SWC: (a_1, a_2) HKW-34-34; (b_1, b_2) HKW-34-51; (c_1, c_2) HKW-51-34; (d_1, d_2) HKW-51-51

occurred on the right sidewall, while a slight buckling deformation occurred on the left sidewall, as shown in Fig. 11(a_1). When σ_Z=150.0 MPa, severe buckling deformation and rock fragment exfoliation occurred on both sidewalls. The failure on both sidewalls approximately penetrated the entire sample along the axis of the hole, as illustrated in Fig. 11(a_2). For sample HKW-34-51, when σ_Z=130.0 MPa, obvious buckling deformation occurred on the right sidewall, while failure did not occur on the left sidewall (Fig. 11(b_1)). When σ_Z= 150.0 MPa, severe buckling deformation and rock fragment exfoliation occurred on the right sidewall. The length of failure along the axis of the hole was approximately 2/3 of the sample length. The left sidewall suffered from obvious buckling deformation, as shown in Fig. 11(b_2). Comparing the failure processes of Samples HKW-34-34 and HKW-34-51 showed that the failure severity of sidewalls was considerably reduced with the increase in the lateral stress under the same vertical stress and horizontal axial stress.

Similarly, the comparison of the failures of Samples HKW-51-34 (Figs. 11(c_1, c_2)) and HKW-51-51 (Figs. 11(d_1, d_2)) showed that, at σ_X= 51.0 MPa and constant vertical stress under SWC, a lower lateral stress led to a more serious sidewall failure. This conclusion is consistent with that at σ_X=34.0 MPa, which indicated reliability and repeatability of the test results. Therefore, the increase in the lateral stress can reduce the failure severity of the surrounding rock of a circular tunnel when the vertical stress and horizontal axial stress are constant under SWC.

4.3 Influence of water content on sidewall failure

To investigate the influence of the water content on the failure of circular hole sidewalls, true-triaxial compression tests were carried out on cubic granite samples with sizes of 100 mm × 100 mm × 100 mm containing a circular through hole with a diameter of 50 mm under SWC. In addition, GONG et al [15] conducted true-triaxial compression tests under NWC using the same material and sample sizes, initial stress state, and loading method. By comparison of the failure processes and characteristics, the influence of the water content on the failure of the circular hole sidewall was studied from three aspects: the failure process, rock fragment characteristics, and failure severity.

According to Fig. 12, the failure process can be divided into four periods under NWC: calm period, particle ejection period, rock fragment exfoliation period, and rock bursting period [15]. Under SWC, the failure process can be divided into four periods: calm period, buckling deformation period, period of rock fragment gradual buckling and exfoliation, and period of formation of symmetrical V-shaped notches, as shown in Fig. 10. In comparison, there were no particle ejection and rock bursting periods under SWC. The failure of the sidewalls was slight, which was a progressive static failure. This indicated that the water reduced the failure severity of circular hole sidewalls, mainly as the water intensified the complexity and randomness of the original microcracks and newly generated cracks, lubricated the joint fracture planes, reduced the cohesion between the mineral particles, and softened the surrounding rock, thus reducing the brittleness and strength of the surrounding rocks.

Figure 13 shows the rock fragments under NWC and SWC. The rock fragments under SWC were larger than those under NWC. In the same

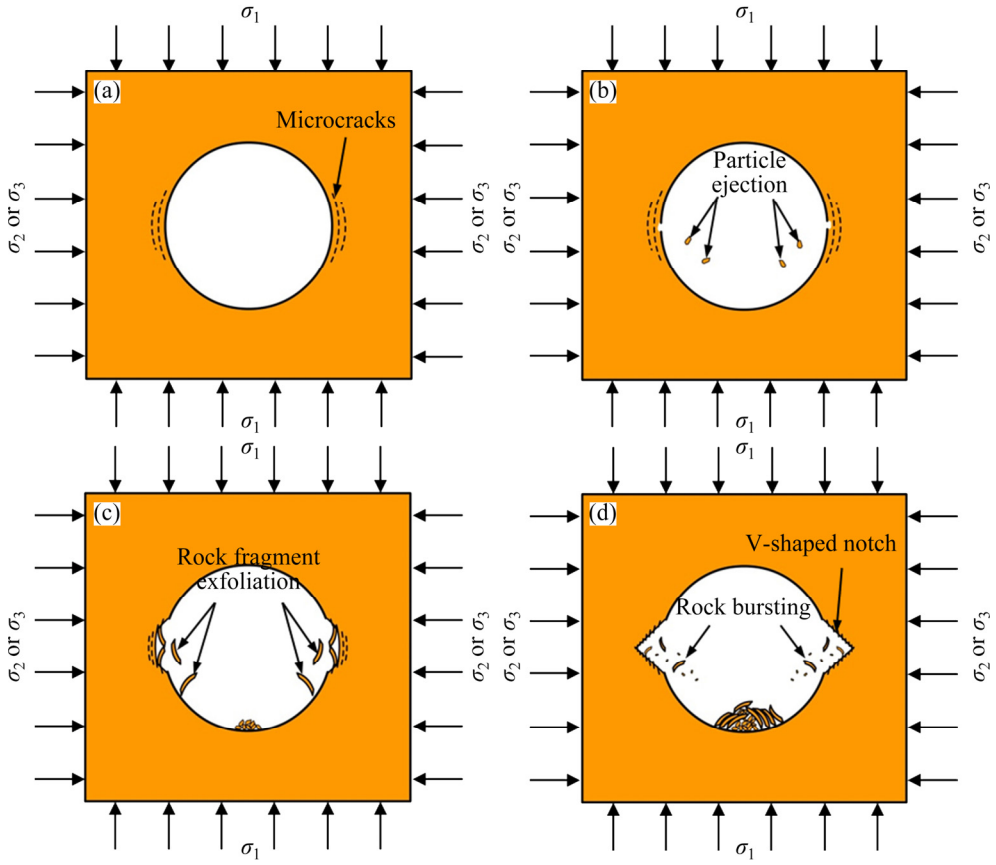

Fig. 12 Schematic diagrams of four periods of sidewall failure under NWC: (a) Calm period; (b) Particle ejection period; (c) Rock fragment exfoliation period; (d) Rock bursting period [15]

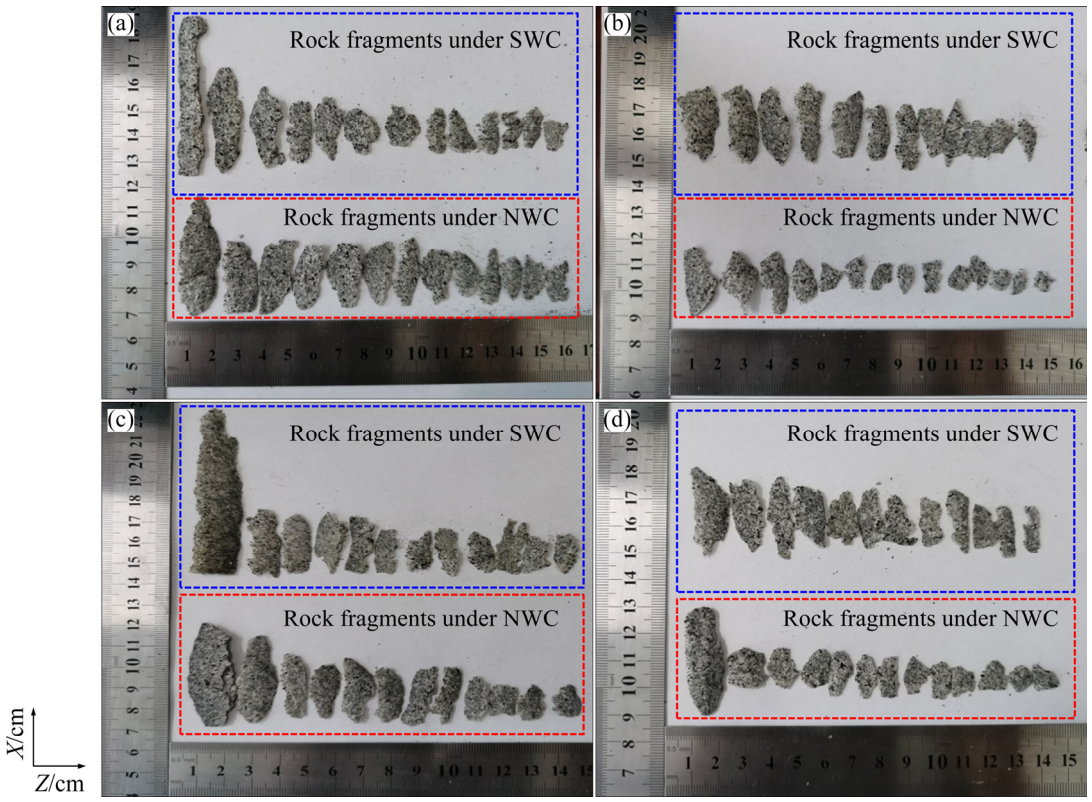

Fig. 13 Comparison of rock fragments under SWC and NWC: (a) HKW-34-34 and HK-34-34; (b) HKW-34-51 and HK-34-51; (c) HKW-51-34 and HK-51-34; (d) HKW-51-51 and HK-51-51

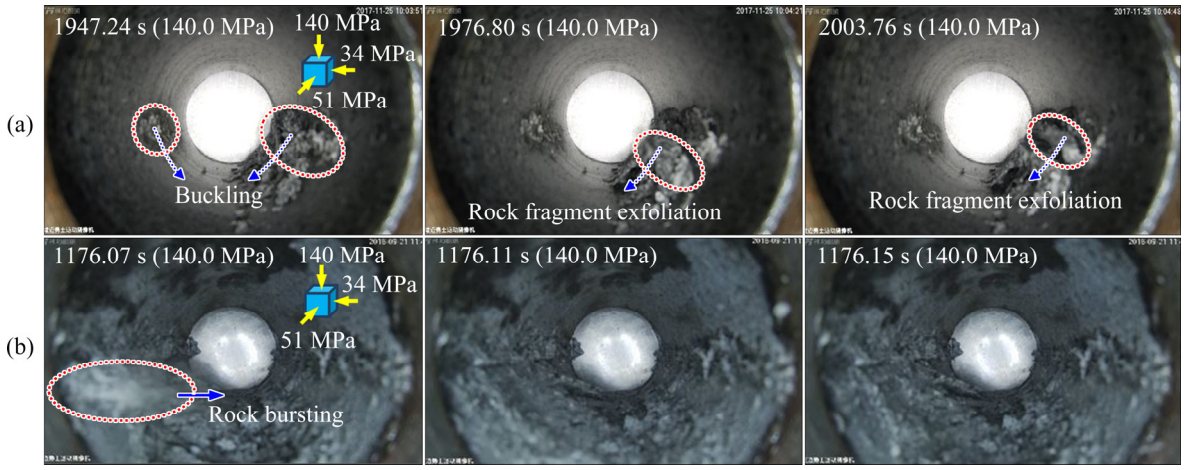

Fig. 14 Failure behaviors of circular hole sidewalls under SWC (a) and NWC (b) [15]

stress states (σ_X=51.0 MPa, σ_Y=34.0 MPa, σ_Z=140.0 MPa), the sidewall under SWC produced buckling deformation and rock fragment exfoliation. As shown in Fig. 14(a), the failure severity was low, with progressive static spalling failure characteristics. Under NWC, substantial rock fragments and fine granite particles were ejected, exhibiting violent dynamic failure with the occurrence of a strong rockburst, as shown in Fig. 14(b) [15]. The comparison results further indicated that the water reduced the failure severity of circular hole sidewalls. In deep underground engineering, water can be used to reduce the failure severity of tunnel surrounding rock, thus reducing the severity and grade of rockburst [27−29], which has a certain guiding significance for the prevention and control of deep rockbursts.

5 Conclusions

(1) Under uniaxial compression, the P-wave velocity under SWC was higher than that under NWC, whereas the average UCS and elastic modulus under SWC were lower than those of granite samples under NWC.

(2) The failure process of the circular hole sidewall under SWC can be divided into four periods: calm period, buckling deformation period, period of rock fragment gradual buckling and exfoliation, and period of formation of symmetrical V-shaped notches.

(3) Under SWC, when the horizontal axial and vertical stresses were constant, a lower lateral stress led to a more serious failure of circular hole sidewalls and larger rock fragments were more prone to form. Therefore, the increase in the lateral stress can reduce the severity of failure of the surrounding rocks.

(4) Under NWC, a strong rockburst with dynamic failure characteristics occurred on the circular hole sidewalls. Under SWC, the circular hole sidewall suffered from spalling failure with progressive static failure characteristics and the failure severity was reduced. Therefore, water can reduce the failure severity of the surrounding rock in deep underground engineering, which has a certain guiding significance for the prevention and control of rockbursts.

Acknowledgments

The authors are grateful for the financial support from the National Natural Science Foundation of China (Nos. 51904335, 41630642).

References

[1] LI Peng, CAI Mei-feng. Challenges and new insights for exploitation of deep underground metal mineral resources [J]. Transactions of Nonferrous Metals Society of China, 2021, 31(11): 3478−3505.

[2] XIE He-ping, XU Wei-lin, LIU Chao, YANG Xing-guo. The subversive idea and key technical prospects on underground hydraulic engineering [J]. Chinese Journal of Rock Mechanics and Engineering, 2018, 37(4): 781−791. (in Chinese)

[3] ZHANG Zhi-zhen, GAO Feng. Experimental investigation on the energy evolution of dry and water-saturated red sandstones [J]. International Journal of Mining Science and Technology, 2015, 25(3): 383−388.

[4] LI Hui-gui, LI Hua-min, XU Guo-sheng. Influence of water

content on mechanical characteristics of weakly cemented sandstone [J]. Journal of Mining and Strata Control Engineering, 2021, 3(4): 043029. (in Chinese)

[5] ZHOU Zi-long, CAI Xin, MA Dan, CAO Wen-zhuo, CHEN Lu, ZHOU Jing. Effects of water content on fracture and mechanical behavior of sandstone with a low clay mineral content [J]. Engineering Fracture Mechanics, 2018, 193: 47−65.

[6] MASOUMI H, HORNE J, TIMMS W. Establishing empirical relationships for the effects of water content on the mechanical behavior of Gosford sandstone [J]. Rock Mechanics and Rock Engineering, 2017, 50: 2235−2242.

[7] ZHOU Zi-long, CAI Xin, ZHAO Yuan, CHEN Lu, XIONG Cheng, LI Xi-bing. Strength characteristics of dry and saturated rock at different strain rates [J]. Transactions of Nonferrous Metals Society of China, 2016, 26(7): 1919−1925.

[8] BAUD P, ZHU W L, WONG T F. Failure mode and weakening effect of water on sandstone [J]. Journal of Geophysical Research (Solid Earth), 2000, 105(B7): 16371−16389.

[9] TAIBI S, DUPERRET A, FLEUREAU J M. The effect of suction on the hydro-mechanical behaviour of chalk rocks [J]. Engineering Geology, 2009, 106(1/2): 40−50.

[10] ZHAO Xing-dong, ZHANG Hong-xun, ZHU Wan-cheng. Fracture evolution around pre-existing cylindrical cavities in brittle rocks under uniaxial compression [J]. Transactions of Nonferrous Metals Society of China, 2014, 24(3): 806−815.

[11] SI Xue-feng, LI Xi-bing, GONG Feng-qiang, HUANG Lin-qi, LIU Xi-ling. Experimental investigation of failure process and characteristics in circular tunnels under different stress states and internal unloading conditions [J]. International Journal of Rock Mechanics and Mining Sciences, 2022, 154: 105116.

[12] SI Xue-feng, LI Xi-bing, GONG Feng-qiang, HUANG Lin-qi, MA Chun-de. Experimental investigation on rockburst process and characteristics of a circular opening in layered rock under three-dimensional stress conditions [J]. Tunnelling and Underground Space Technology, 2022, 127: 104603.

[13] ZHAO Hua-tao, TAO Ming, LI Xi-bing, HITOSHI M, XU Shi-bo. Influence of excavation damaged zone on the dynamic response of circular cavity subjected to transient stress wave [J]. International Journal of Rock Mechanics and Mining Sciences, 2021, 142: 104708.

[14] GONG Feng-qiang, LUO Yong, LI Xi-bing, SI Xue-feng, TAO Ming. Experimental simulation investigation on rockburst induced by spalling failure in deep circular tunnels [J]. Tunnelling and Underground Space Technology, 2018, 81: 413−427.

[15] GONG Feng-qiang, SI Xue-feng, LI Xi-bing, WANG Shan-yong. Experimental investigation of strain rockburst in circular caverns under deep three-dimensional high-stress conditions [J]. Rock Mechanics and Rock Engineering, 2019, 52(5): 1459−1474.

[16] SI Xue-feng, HUANG Lin-qi, LI Xi-bing, GONG Feng-qiang, LIU Xi-ling. Mechanical properties and rockburst proneness of phyllite under uniaxial compression [J]. Transactions of Nonferrous Metals Society of China, 2021, 31(12): 3862−3878.

[17] SI Xue-feng, GONG Feng-qiang. Strength-weakening effect and shear-tension failure mode transformation mechanism of rockburst for fine-grained granite under triaxial unloading compression [J]. International Journal of Rock Mechanics and Mining Sciences, 2020, 131: 104347.

[18] HU Xiao-chuan, SU Guo-shao, LI Zhen-yu, XU Chao-shui, YAN Xiao-yang, LIU Yan-xin, YAN Liu-bin. Suppressing rockburst by increasing the tensile strength of rock surface: An experimental study [J]. Tunnelling and Underground Space Technology, 2021, 107: 103645.

[19] MIRONENKO V, STRELSKY F. Hydrogeomechanical problems in mining [J]. Mine Water and the Environment, 1993, 12(1): 35−40.

[20] FOWKES N. Rockbursts mud and plastic [C]//Proceedings of the 19th International Congress on Modelling and Simulation. Perth, Australia: Modelling and Simulation Society of Australia and New Zealand, 2011: 304−310.

[21] LUO Yong. Influence of water on mechanical behavior of surrounding rock in hard-rock tunnels: An experimental simulation [J]. Engineering Geology, 2020, 277: 105816.

[22] SI Xue-feng, HUANG Lin-qi, LI Xi-bing, MA Chun-de, GONG Feng-qiang. Experimental investigation of spalling failure of D-shaped tunnel under three-dimensional high-stress conditions in hard rock [J]. Rock Mechanics and Rock Engineering, 2021, 54: 3017−3038.

[23] GONG Feng-qiang, WU Wu-xing, LI Tian-bin, SI Xue-feng. Experimental simulation and investigation of spalling failure of rectangular tunnel under different three-dimensional stress states [J]. International Journal of Rock Mechanics and Mining Sciences, 2019, 122: 104081.

[24] BROWN E T, HOEK E. Trends in relationships between measured in-situ stresses and depth [J]. International Journal of Rock Mechanics and Mining Sciences & Geomechanics Abstracts, 1978, 15(4): 211−215.

[25] STEPHANSSON O, SÄRKKÄ P, MYRVANG A. State of stress in Fennoscandia [C]//Proceedings on Rock Stress and Rock Stress Measurement. Stockholm, 1986: 21−32.

[26] LUO Song, GONG Feng-qiang. Linear energy storage and dissipation laws during rock fracture under three-point flexural loading [J]. Engineering Fracture Mechanics, 2020, 234: 107102.

[27] FRID V. Electromagnetic radiation method water-infusion control in rockburst-prone strata [J]. Journal of Applied Geophysics, 2000, 43(1): 5−13.

[28] LIU Xiang-xin, LIANG Zheng-zhao, ZHANG Yan-bo, LIANG Peng, TIAN Bao-zhu. Experimental study on the monitoring of rockburst in tunnels under dry and saturated conditions using AE and infrared monitoring [J]. Tunnelling and Underground Space Technology, 2018, 82: 517−528.

[29] SONG Da-zhao, WANG En-yuan, LIU Zhen-tang, LIU Xiao-fei, SHEN Rong-xi. Numerical simulation of rock-burst relief and prevention by water-jet cutting [J]. International Journal of Rock Mechanics and Mining Sciences, 2014, 70: 318−331.

饱和含水量下三维高应力圆形隧道的破坏过程及特征

司雪峰[1]，黄麟淇[1]，宫凤强[2]，李夕兵[1]

1. 中南大学 资源与安全工程学院，长沙 410083;
2. 东南大学 土木工程学院，南京 211189

摘　要：采用真三轴试验系统对含圆形贯穿孔洞的立方体花岗岩试样进行真三轴压缩试验，研究饱和含水量(SWC)对圆形隧道围岩破坏过程和特征的影响。SWC 条件下板裂化破坏可分为 4 个阶段：平静阶段、屈曲变形阶段、岩片逐渐屈曲和剥落阶段及形成对称的 V 型槽阶段。当水平轴向应力和垂直应力保持不变时，板裂化破坏的严重程度随着侧向应力的增加而降低。在自然含水量条件下，圆形孔洞边墙发生具有动态破坏特征的强岩爆；在 SWC 条件下，破坏的严重程度降低，圆形孔洞围岩发生板裂化破坏，表现出渐进的静态破坏特征。因此，在深部地下工程中，水可以降低围岩破坏的严重程度，对岩爆防治具有一定的指导意义。

关键词：深部硬岩；圆形隧道；饱和含水量；岩爆；板裂化破坏；三维高应力；V 型槽

(Edited by Wei-ping CHEN)